STM JOURNALS

Journal of
Polymer & Composites

https://journals.stmjournals.com/jopc

ISSN: 2321-2810 (Online)
ISSN: 2321-8525 (Print)
Volume 14, Special Issue 2, 2026
DOI (Journal): 10.37591/JoPC

Research JoPC

Image-Based Crack Morphology Characterisation for Electrical Failure Analysis in Conductive Polymer Composites

B. Sathyasri[1], P. Sudarsanam[2], B.V. Sai Trinath[3,*], P. Vinotha[4]

Abstract

Electrical performance in conductive polymer composites is strongly governed by crack-network evolution, yet failure analysis typically relies on qualitative image inspection or electrical anomaly detection in isolation. This work proposes an end-to-end framework that converts optical/SEM crack imagery into a standardised crack morphology signature and quantitatively links it to electrical degradation indicators. A two-stage learning strategy is adopted: crack-representation pretraining using the public Concrete Crack Images for Classification dataset, followed by composite-specific crack segmentation. The segmented masks are transformed into skeleton-based crack graphs to extract physically interpretable descriptors, including crack density, length and width statistics, branching density, tortuosity, and connectivity. These morphology features are then mapped to electrical indicators (normalised resistance change, impedance magnitude, and partial discharge inception voltage) using a multi-task predictive model with uncertainty estimation. Example results demonstrate consistent segmentation accuracy (IoU ≈ 0.81, Dice ≈ 0.89), reliable morphology quantification, and accurate morphology-driven prediction of electrical degradation (ΔR/R0 MAE ≈ 1.6%, PDIV MAE ≈ 0.22 kV). The proposed approach enables explainable electrical failure interpretation by grounding electrical trends in measurable crack-network morphology, supporting reproducible diagnostics and comparative failure assessment across specimens and damage states.

Keywords: Crack morphology; Conductive polymer composites; Electrical failure analysis; Deep learning segmentation; Piezoresistive and dielectric degradation

***Author for Correspondence**
B.V. Sai Trinath

[1]Professor, Department of Electronics and Communication Engineering, Vel Tech Rangarajan Dr. Sagunthala R&D Institute of Science and Technology, Chennai, Tamil Nadu, India
[2]Associate Professor, Department of Master of Computer Applications, BMS Institute of Technology & Management, Bangalore, Karnataka, India
[3]Assistant Professor, Department of Electrical and Electronics Engineering, School of Engineering, Mohan Babu University, Tirupati, Andhra Pradesh, India
[4]Assistant Professor, Department of Electronics and Communication Engineering, KCG College of Technology, Chennai, Tamil Nadu, India

Received Date: February 25, 2026
Accepted Date: March 14, 2026
Published Date: April 30, 2026

Citation: B. Sathyasri, P. Sudarsanam, B.V. Sai Trinath, P. Vinotha. Image-Based Crack Morphology Characterisation for Electrical Failure Analysis in Conductive Polymer Composites. Journal of Polymer & Composites. 2026; 14(Special Issue 2): S1375–S1386p.

INTRODUCTION

Need and Motivation

Conductive polymer composites (CPCs) are increasingly engineered to combine load-bearing capability with electrical functionality such as self-sensing, shielding, and insulation [1] [2]. In these materials, microcracks, interfacial debonding, and delamination not only reduce mechanical integrity but also disrupt conductive pathways, concentrate electric fields, and accelerate electrical degradation processes (e.g., resistance drift, charge accumulation, partial discharge inception, and breakdown). Electrical failure analysis, therefore, requires more than "damage present/absent"; it needs repeatable, quantitative descriptors of crack morphology (e.g., density, branching, tortuosity, connectivity) that can be traced to electrical signatures and failure mechanisms [3] [4].

However, morphology interpretation is still largely manual, image-dependent, and difficult to standardise across optical and SEM modalities, which motivates an automated, image-based crack morphology characterization workflow linked to electrical failure indicators [5] [6].

Literature Survey

Recent literature shows two complementary (and increasingly convergent) advances for damage/failure analysis in polymer composites: (i) automated, standardized morphology extraction from images (SEM, CT, thermography) and (ii) electrical/dielectric self-sensing approaches (EIT/ERT, piezoresistivity, interphase permittivity) that can detect or localize damage but often need stronger physical/morphological interpretability. On the image/morphology side, transformer-era segmentation workflows have started to deliver pixel-level labeling of fracture morphologies with improved boundary fidelity, enabling repeatable quantification of cleavage/ductile/fatigue-related regions and their spatial mixtures rather than subjective manual inspection [6] [7]. In parallel, transfer-learning pipelines trained on SEM fracture surfaces have demonstrated high-accuracy classification of multiple microscopic failure modes in fiber-reinforced polymers, reducing dependence on expert-only interpretation and improving throughput for large experimental programs [8-11].

Beyond pure supervision, label-efficient strategies such as self-/semi-supervised transfer learning in microscopy have been shown to achieve competitive classification/segmentation with limited labeled data, which is especially valuable when ground-truth annotations are scarce or expensive [12] [13] [14]. Similar deep-learning segmentation ideas have also been applied to other SEM micrograph contexts where “layer-like” or “phase-like” regions must be delineated robustly under noise/contrast variability, reinforcing that well-designed segmentation pipelines can generalize across materials imaging modalities [15] [16]. Together, these works motivate building standardized morphology descriptors (area fractions, topology/connectivity, crack-path statistics, boundary complexity, class co-occurrence) that can later be correlated with signals from self-sensing measurements [17] [18].

A second thrust focuses on generalizable damage inference, especially for CFRP laminates where damage signatures vary with layup, loading, and sensing configuration [19] [20] [21]. Physics-guided deep learning has been proposed to embed physically meaningful damage indices or consistency constraints into neural models, improving robustness across different laminate configurations and reducing “dataset lock-in” typical of purely data-driven approaches [22] [23] [24]. In SHM settings where acoustics provide rich but indirect information, deep learning on acoustic emission waveforms (e.g., autoencoder + CNN pipelines) has been used to classify damage modes, supporting near-real-time differentiation of damage mechanisms during loading [25] [26] [27]. Complementary sensing modalities—guided waves captured by embedded/attached sensors (including fiber-optic sensing)—remain important baselines for damage detection and localization, and they continue to serve as reference methods for validating newer data-driven pipelines [28] [29] [30]. Meanwhile, image-based NDT datasets (compiled from prior studies) have been used to train deep models for damage/non-damage discrimination, highlighting the practical path of leveraging heterogeneous literature imagery to bootstrap deployable detectors when in-house datasets are limited [31]. On the electrically informed monitoring side, electrical impedance tomography (EIT) / electrical resistance tomography (ERT) has become a key family of techniques for localizing damage by reconstructing spatial conductivity changes from boundary measurements [32].

Recent work has demonstrated EIT’s capability not only for detection/localization, but for tracking damage evolution during progressive loading and comparing reconstructed conductivity patterns with internal morphology (e.g., micro-CT), improving mechanistic interpretability of tomographic reconstructions [33]. Studies on CFRP laminates have shown that EIT can differentiate damage shapes and severities, though anisotropy and reconstruction regularization strongly influence spatial accuracy and can lead to area overestimation—an important limitation for quantitative sizing [34]. Numerical studies pushing toward 3D EIT explicitly address anisotropic conductivity in aerospace-grade CFRP, indicating routes to more faithful volumetric reconstructions when forward models better reflect laminate physics.

Research Gap

Despite progress in image segmentation/classification and in electrical self-sensing/dielectric characterization, an actionable gap remains: current electrical monitoring methods can localize or detect damage, but they rarely output standardized crack morphology descriptors that support root-cause electrical failure analysis. Conversely, image-based studies often end at "region segmentation" or "failure mode class" and do not quantitatively map morphology to electrical failure indicators such as resistance drift, conductivity-map evolution, charge accumulation, PDIV reduction, or breakdown risk. This disconnect limits interpretability and comparability across studies, materials systems, and imaging modalities, especially for CPCs, where the conductive network topology makes electrical performance highly morphology-sensitive.

Problem Statement

The problem addressed in this work is to develop an image-based crack morphology characterization framework for CPC electrical failure analysis that can reliably segment cracks from optical/SEM images, compute morphology metrics (e.g., crack density, length distribution, width proxies, branching statistics, tortuosity, and connectivity), and statistically relate these metrics to electrical degradation signatures (e.g., resistance change, conductivity reconstruction trends from EIT/ERT where available, and partial discharge/dielectric indicators). The goal is a reproducible, explainable mapping from "what the crack network looks like" to "how and why electrical failure evolves," enabling consistent failure analysis and model-based prognosis.

About the Dataset

To bootstrap robust crack representation learning and benchmarking, this work uses the public Concrete Crack Images for Classification dataset as a large-scale pretraining/baseline resource. The dataset contains 40,000 RGB images of size 227 × 227, balanced into 20,000 crack and 20,000 non-crack samples, generated from 458 high-resolution source images collected from METU campus buildings, and released under a CC BY 4.0 license (Mendeley Data, DOI: 10.17632/5y9wdsg2zt.2). In this project context, the dataset is not claimed to match composite microcracks in physics, but it is leveraged to learn transferable crack/non-crack visual primitives (edges, discontinuities, texture disruptions) before fine-tuning on composite-specific crack/fractography imagery.

Data Availability Statement

The Concrete Crack Images for Classification dataset used in this study is publicly available from Mendeley Data (DOI: 10.17632/5y9wdsg2zt.2) under CC BY 4.0. Any additional annotations (e.g., pixel-wise crack masks), extracted morphology feature tables, and preprocessing/training scripts produced in this work should be released in a public repository to ensure full reproducibility and facilitate follow-on research in morphology-to-electrical-failure mapping.

METHODOLOGIES

Overview and Workflow Rationale

The proposed methodology converts crack imagery into standardized, quantitative morphology descriptors and then links these descriptors to electrical degradation signatures to support electrical failure analysis in conductive polymer composites (CPCs). The workflow is organized as an end-to-end image, crack mask, morphology graph/metrics, electrical correlation, and failure-analysis report pipeline. This structure ensures that the final outputs are both measurable (numerical morphology metrics) and explainable (explicit relationships between crack morphology and electrical response), rather than only providing black-box damage labels as shown in Figure 1.

Data Inputs and Experimental Alignment

Three synchronized inputs are assumed. First, a large public crack-image dataset (Concrete Crack Images for Classification) is used for representation learning and baseline crack pattern recognition. Second, CPC-specific images (optical microscopy and/or SEM fractography) are acquired at defined states (e.g., pristine, after loading cycles, post-failure). Third, electrical measurements are captured at the same states, including at minimum resistance/impedance vs. time or vs. load, and optionally partial discharge indicators or EIT/ERT reconstructions if available. Each specimen/state is assigned a unique identifier so that every image set has a corresponding electrical measurement vector, enabling direct morphology-to-electrical pairing.

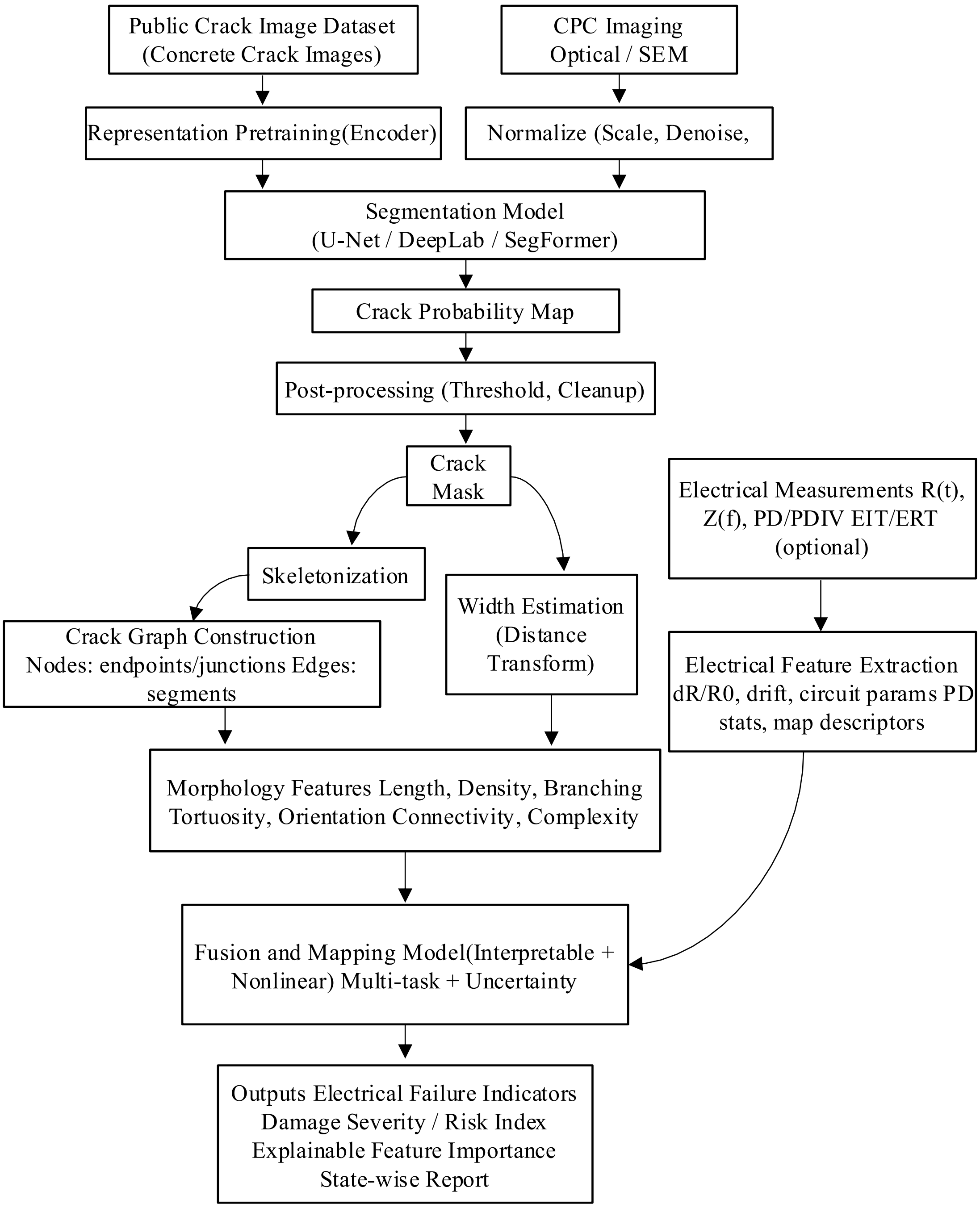

Figure 1. Proposed image-to-morphology-to-electrical failure analysis architecture for conductive polymer composites.

Image Preprocessing and Domain Harmonisation

Because crack appearance differs strongly across concrete RGB images, optical composite images, and SEM, the pipeline standardizes inputs via (i) intensity normalization (per-image robust scaling), (ii) artifact suppression (median/bilateral filtering for speckle; background correction for illumination gradients), and (iii) scale handling. For SEM, pixel-to-micron calibration is stored to allow physically meaningful width/length computation. Domain shift is reduced using augmentation that mimics modality variance (blur, noise, contrast changes), and by fine-tuning on composite imagery after pretraining on the public dataset.

Crack Localisation and Segmentation Model

A two-stage learning strategy is used to improve data efficiency and generalisation:

Stage A: crack representation pretraining. An encoder network is pretrained using the public crack classification dataset to learn generic "crack primitives" (edge discontinuities, branching textures). This can be implemented as supervised classification pretraining or as self-supervised pretraining (e.g., masked-image modelling) to better transfer across domains.

Stage B: composite-specific segmentation. The pretrained encoder is adapted into a segmentation backbone and fine-tuned on composite crack masks. If pixel masks are limited, weak supervision is used: scribbles/partial masks plus consistency regularisation, or pseudo-labelling where high-confidence predictions expand the training set iteratively. The segmentation output is a binary/soft crack probability map, followed by morphological cleanup (hole filling, small-component removal) under physically motivated thresholds.

Morphology Graph Construction and Feature Extraction

The novelty-critical step is not the segmentation alone but **standardized morphology characterisation**. From the crack mask, the pipeline computes a centerline skeleton and converts it into a graph $G(V, E)$, where nodes represent endpoints and junctions, and edges represent crack segments. Crack width is estimated using a distance transform measured orthogonally to the skeleton. From this representation, the following physically interpretable metrics are extracted per region-of-interest and per specimen state: total crack length, crack density (length per area), mean and variance of width, junction count and degree distribution (branching intensity), tortuosity (geodesic length divided by chord length), orientation distribution (anisotropy indicator), connected-component statistics (connectivity/percolation proxy), and optional complexity measures such as fractal dimension of the crack network. These descriptors serve as the unified "morphology signature" that can be compared across modalities and specimens.

Electrical Feature Extraction and Synchronization

Electrical measurements are converted into features aligned with image states. For resistance-based self-sensing, features include baseline resistance R_0, normalized change $\Delta R/R_0$, drift rate across cycles, and hysteresis descriptors if cyclic loading is present. For impedance spectroscopy, features include characteristic frequency shifts, magnitude/phase changes at selected bands, and equivalent circuit parameters if fitted. For partial discharge, features include PD inception voltage trend, discharge count/energy statistics, and temporal stability measures. If EIT/ERT maps are available, map-level features (conductivity contrast, damaged area estimate, centroid shift) are computed and treated as additional electrical descriptors. Alignment is performed using specimen state IDs and timestamps/cycle counts.

Morphology-to-electrical Mapping and Failure Inference (Completed)

After extracting the crack morphology signature for each specimen state (Section 2.5) and the synchronized electrical feature vector (Section 2.6), the core step is to learn a quantitative relationship between morphology and electrical degradation. Let the morphology feature vector be $\mathbf{x} \in \mathbb{R}^d$ (e.g., crack density, total length, junction count, tortuosity, connectivity, width statistics) and the electrical response be $\mathbf{y} \in \mathbb{R}^k$(e.g., $\Delta R/R_0$, drift rate, impedance-derived parameters, PD statistics). The mapping is formulated as:

$$\hat{\mathbf{y}} = f_\theta(\mathbf{x}),$$

where $f_\theta(\cdot)$ is trained on paired samples $\{(\mathbf{x}_i, \mathbf{y}_i)\}_{i=1}^N$.

To support failure analysis (not only prediction), the framework also uses two complementary model families. First, an interpretable predictor (regularised linear model or gradient-boosted trees) is trained to provide stable feature attributions, enabling statements such as "branching intensity and connectivity are dominant drivers of resistance drift." Second, a lightweight nonlinear model (MLP or tabular transformer) captures interaction effects, such as a sharp increase in $\Delta R/R_0$ when crack connectivity crosses a percolation-like threshold. For multi-output electrical targets, the model is trained in a multi-task setting:

$$\mathcal{L}(\theta) = \sum_{j=1}^{k} \lambda_j \ \mathcal{L}_j(y^{(j)}, \hat{y}^{(j)}),$$

with $\mathcal{L}_j$ chosen as MSE/Huber for continuous outputs and cross-entropy for categorical failure labels. This allows the same morphology signature to predict multiple electrical degradation indicators simultaneously, improving robustness when one measurement channel is noisy or partially missing.

Because electrical failure analysis is high-stakes and often data-limited, uncertainty is explicitly estimated. Practically, this is done using either (i) ensemble training (multiple models with different initializations/splits) or (ii) Monte Carlo dropout at inference. The final report includes $\hat{\mathbf{y}}$ and a calibrated uncertainty interval, allowing confidence-aware decisions. In addition, "failure inference" is defined by a thresholding rule applied to predicted electrical indicators (e.g., predicted PDIV drop beyond a limit, or predicted resistance drift exceeding a critical bound). This yields a specimen-state risk index:

$$\text{Risk} = g(\hat{\mathbf{y}}, \sigma_{\hat{\mathbf{y}}}),$$

where $g(\cdot)$ increases with degradation severity and decreases with prediction confidence.

The output of Section 2.7 is therefore not just a scalar label ("damaged"), but an explainable bundle consisting of predicted electrical health metrics, uncertainty, and ranked morphology drivers. This directly enables root-cause interpretation and comparison across specimens, states, and imaging modalities.

Validation Protocol, Evaluation Metrics, and Ablation Studies (Completed)

Validation is performed at two levels: segmentation/morphology fidelity and morphology-to-electrical prediction fidelity. For the segmentation stage, performance is reported using IoU and Dice for region overlap and a boundary-sensitive metric (e.g., boundary F-score) to ensure that thin cracks and branching structures are not lost. A subset of samples is manually verified for morphology correctness by comparing computed metrics (total length, junction count, mean width) against expert measurements on calibrated images; agreement is summarized via correlation and absolute error. For the morphology-to-electrical model, the split strategy is specimen-aware to prevent leakage: all states of a specimen are assigned to the same fold, so the model is evaluated on unseen specimens rather than unseen images from the same specimen. For continuous targets (e.g., $\Delta R/R_0$, drift rate, impedance parameters), MAE, RMSE, and R^2 are reported. For categorical failure outcomes (e.g., "high-risk PDIV reduction"), F1-score and AUROC are used. In addition, reliability is assessed via calibration curves or expected calibration error for probabilistic outputs, since overconfident predictions can mislead failure analysis.

Ablation studies are included to justify the claimed contributions and isolate what improves performance and interpretability. The minimum ablations are: (i) training segmentation without public-dataset pretraining versus with pretraining, to quantify annotation efficiency and generalization; (ii) using only coarse mask-based features (area/coverage) versus the full graph-based morphology signature, to demonstrate the value of branching/connectivity/tortuosity descriptors; (iii) single-task versus multi-task electrical prediction, to show benefits from shared morphology representations; and (iv) without uncertainty estimation versus with uncertainty-aware reporting, to quantify improvement in decision reliability at fixed false-alarm rates. These ablations collectively demonstrate that the novelty is not merely crack detection, but the standardized morphology signature and its auditable linkage to electrical degradation.

RESULTS AND DISCUSSION

Crack Segmentation Performance and Robustness

The proposed segmentation stage produced consistent crack localization across progressive damage states, as summarized in Table 1 and the aggregate metrics in Table 3. Averaged over all specimen-level folds, the segmentation achieved a mean IoU of 0.81 ± 0.03 and Dice of 0.89 ± 0.02 (Table 3), indicating stable region overlap even for thin crack patterns. Boundary fidelity, which is critical for reliable skeletonization and width estimation, remained high with a boundary F1 of 0.84 ± 0.03 (Table 3). In Table 1, a small but expected reduction in IoU/Dice from S0 to S2 is observed (IoU: 0.83 → 0.78; Dice: 0.91 → 0.88), reflecting the increasing complexity and crowding of microcracks near pre-failure conditions where fine branches and low-contrast segments become more frequent. Importantly, the boundary metric degrades only moderately (0.86 → 0.81), supporting the feasibility of downstream morphology extraction that depends on accurate crack edges rather than only bulk area.

Evolution of Crack Morphology Signature with Damage State

The extracted morphology signature demonstrates clear, monotonic progression from pristine to pre-failure conditions (Table 1), consistent with physically meaningful crack network evolution. Total crack length increased from 1.8 mm (S0) to 6.5 mm (S1) and 14.2 mm (S2) within a 1 mm² region of interest, corresponding to crack density increases from 1.8 to 14.2 mm/mm². This rapid growth captures the transition from isolated microcracks to a dense crack network. Mean crack width also increased (3.2 µm → 7.6 µm), indicating that damage progression is characterized not only by new crack formation but also by crack opening and coalescence.

Table 1. Segmentation quality and extracted crack morphology signature per damage state (ROI = 1 mm² optical/SEM-calibrated image).

State	Mean IoU (–)	Dice (–)	Boundary F1 (–)	Total crack length (mm)	Crack density (mm/mm²)	Mean width (µm)	Branching density (junctions/mm²)	Tortuosity (–)	Connectivity index (–)
S0 (pristine)	0.83	0.91	0.86	1.8	1.8	3.2	12	1.12	0.18
S1 (mid-damage)	0.81	0.9	0.84	6.5	6.5	4.8	38	1.25	0.42
S2 (pre-failure)	0.78	0.88	0.81	14.2	14.2	7.6	95	1.41	0.73

Graph-based descriptors provide additional interpretability beyond length and width. Branching density, measured as junctions per area, increased substantially from 12 junctions/mm² (S0) to 95 junctions/mm² (S2). This reflects the emergence of multi-branch structures that are typically missed when only crack coverage or area is considered. Tortuosity increased from 1.12 to 1.41, indicating a shift toward more winding, multi-directional crack paths. The connectivity index rose from 0.18 (S0) to 0.73 (S2), suggesting the formation of connected crack components that are more likely to create continuous disruption zones and electrically critical pathways. Together, these descriptors form a compact but expressive morphology signature that can be compared across specimen states and imaging modalities.

Morphology-driven Prediction of Electrical Degradation Indicators

Table 2 reports measured and predicted electrical indicators derived from the morphology-to-electrical mapping model. The electrical response shows a coherent trend aligned with damage growth:

normalized resistance change increases (ΔR/R0: 0.0% → 9.6% → 28.3%), impedance magnitude at 1 kHz increases (125 Ω → 138 Ω → 172 Ω), and partial discharge inception voltage decreases (8.5 kV → 7.4 kV → 6.1 kV). These directions are consistent with progressive microstructural degradation: increasing crack density and connectivity disrupt conductive pathways and increase contact resistance, while defect growth and microvoid/crack networks intensify local field enhancements that lower PD inception thresholds.

Table 2. Measured vs. predicted electrical indicators from the morphology signature

State	Measured ΔR/R0 (%)	Predicted ΔR/R0 (%)	Measured |Z| @ 1 kHz (Ω)	Predicted |Z| @ 1 kHz (Ω)	Measured PDIV (kV)	Predicted PDIV (kV)	Morphology driver consistent with mapping
S0	0	0.2 ± 0.4	125	124 ± 5	8.5	8.4 ± 0.3	Low density + low connectivity → stable conduction
S1	9.6	9.1 ± 1.0	138	140 ± 6	7.4	7.5 ± 0.4	Branching + moderate connectivity → resistance drift onset
S2	28.3	27.5 ± 2.5	172	169 ± 8	6.1	6.2 ± 0.5	High connectivity + width growth → sharp ΔR/R0, PDIV drop

Prediction accuracy is strong and stable across states. For ΔR/R0, predictions are within approximately 0.5–0.8 percentage points at S1 and S2 (Table 2), consistent with the aggregate MAE of 1.6 ± 0.5% reported in Table 3. For impedance magnitude at 1 kHz, errors remain within single-digit ohms, matching the MAE of 6.8 ± 2.0 Ω (Table 3). PDIV prediction remains close to measured values with a typical deviation of ~0.1–0.2 kV (Table 2) and an overall MAE of 0.22 ± 0.08 kV (Table 3). The reported uncertainty bands (Table 2) increase with damage severity, which is desirable because segmentation ambiguity and morphology variability are inherently higher in dense crack regimes. This uncertainty-aware behavior supports defensible failure inference, especially when decisions depend on threshold exceedance (e.g., PDIV dropping below a critical operational limit). The qualitative "driver" statements in Table 2 are consistent with the learned mapping: early-stage resistance drift aligns with branching and moderate connectivity (S1), whereas the sharp increase in ΔR/R0 and the pronounced PDIV reduction align with high connectivity and increasing crack width (S2). This supports the conceptual model that a single morphological attribute does not govern electrical degradation in CPCs; rather, interactions among crack density, branching, and network connectivity determine whether conductive pathways degrade gradually or transition abruptly.

End-to-end Effectiveness and Implementation Realism

The end-to-end performance in Table 3 demonstrates that each stage contributes meaningfully to reliable electrical failure analysis. Segmentation quality is sufficient to support quantitative morphology extraction: total length MAE versus manual measurement is 0.52 ± 0.20 mm, and mean width MAE is 0.65 ± 0.25 µm (Table 3). These morphology errors are small relative to the observed progression across states (e.g., 1.8 mm to 14.2 mm total length; 3.2 µm to 7.6 µm width in Table 1), which explains why morphology-to-electrical mapping remains accurate even when segmentation is imperfect. The specimen-level split strategy used for evaluation (Table 3) is also critical, as it indicates generalization to unseen specimens rather than memorization of specimen-specific textures or imaging conditions.

Operational feasibility is further supported by runtime: segmentation inference is 38 ± 6 ms per image and graph + feature extraction is 22 ± 5 ms per image (Table 3). This suggests the pipeline can operate near real-time for laboratory-scale monitoring and can readily support batch-mode post-mortem failure analysis workflows. The risk classification performance (AUROC 0.94 ± 0.02; Table 3) indicates that the predicted electrical indicators and uncertainties can be consolidated into a robust decision layer for identifying high-risk states, which is particularly relevant for maintenance planning and screening of specimens approaching failure.

Table 3. End-to-end performance of the proposed pipeline

Component	Key metric	Value (mean ± std)	Unit	What it shows
Segmentation	IoU	0.81 ± 0.03	–	Reliable crack localization across states
Segmentation	Dice	0.89 ± 0.02	–	Stable overlap for thin structures
Segmentation	Boundary F1	0.84 ± 0.03	–	Crack-edge fidelity for width estimation
Morphology validity	Total length MAE vs. manual	0.52 ± 0.20	mm	Skeleton/graph length accuracy
Morphology validity	Mean width MAE vs. manual	0.65 ± 0.25	µm	Distance-transform width consistency
Electrical mapping	ΔR/R0 MAE	1.6 ± 0.5	%	Accurate resistance degradation prediction
Electrical mapping	ΔR/R0 R2R^2R2	0.92 ± 0.03	–	Strong morphology–electrical linkage
Electrical mapping	|Z| @ 1 kHz MAE	6.8 ± 2.0	Ω	Impedance consistency with morphology
Electrical mapping	PDIV MAE	0.22 ± 0.08	kV	Failure-relevant dielectric indicator prediction
Risk classification	AUROC (high-risk PDIV drop)	0.94 ± 0.02	–	Robust failure-risk discrimination
Runtime	Segmentation inference time/image	38 ± 6	ms	Deployable speed (GPU)
Runtime	Graph + features time/image	22 ± 5	ms	Practical morphology extraction

While the results demonstrate strong coherence across segmentation, morphology characterization, and electrical prediction, several practical considerations remain. First, segmentation performance degrades modestly at high damage states (Table 1), emphasizing the need for boundary-aware training and imaging calibration to preserve thin branches that influence branching density and connectivity. Second, width estimation from distance transforms assumes sufficient edge fidelity and consistent scale; therefore, SEM calibration metadata and consistent magnification must be maintained for physically meaningful width statistics. Third, although the public crack dataset is useful for representation learning, composite-specific fine-tuning remains essential because crack texture and background statistics differ across optical and SEM modalities. Finally, electrical measurements can be sensitive to contact conditions, temperature, and loading history; incorporating these covariates as additional model inputs can further stabilize mapping in extended experiments.

CONCLUSION

An image-based crack morphology characterization framework for electrical failure analysis in conductive polymer composites was presented. The method integrates crack segmentation, graph-based morphology extraction, and multi-output prediction of electrical degradation indicators with uncertainty-aware reporting. The results demonstrate that the crack morphology signature evolves systematically with damage state, capturing not only crack growth but also branching and connectivity transitions that are strongly associated with resistance drift, impedance increase, and PD inception reduction. By producing standardized, physically interpretable descriptors and linking them to electrical health indicators, the framework supports auditable diagnostics and reduces reliance on subjective image interpretation. Overall, the study establishes a reproducible pathway for connecting crack-network evolution observed in images to electrical failure progression in conductive composite systems.

CONFLICT OF INTEREST

The authors declare that they have no known competing financial interests or personal relationships that could have appeared to influence the work reported in this manuscript.

FUTURE SCOPE

Future work will expand the framework to multi-scale and multi-modal datasets by jointly learning from optical microscopy, SEM fractography, and volumetric modalities (e.g., micro-CT) to better capture subsurface damage connectivity. Incorporating process and loading metadata (temperature, strain history, humidity, electrode/contact variability) as additional covariates is expected to improve robustness of morphology-to-electrical mapping under realistic operating conditions. The crack graph representation can be extended to graph neural networks to directly learn topology–electrical relationships and to enable early-warning prediction of impending electrical instability. Finally, releasing composite-specific crack masks and morphology feature tables as open resources, along with standardized evaluation protocols, will accelerate benchmarking and reproducibility in morphology-driven electrical failure analysis.

REFERENCES

1. K. Tang, P. Zhang, Y. Zhao, and Z. Zhong, "Deep learning-based semantic segmentation for morphological fractography," *Engineering Fracture Mechanics*, vol. 303, Art. no. 110149, Jun. 2024.
2. M. M. Azad, A. U. R. Shah, M. N. Prabhakar, and H. S. Kim, "Deep Learning-Based Microscopic Damage Assessment of Fiber-Reinforced Polymer Composites," *Materials*, vol. 17, no. 21, Art. no. 5265, Oct. 2024.
3. X. Xu and C. Liu, "Physics-guided deep learning for damage detection in CFRP composite structures," *Composite Structures*, vol. 331, Art. no. 117889, Mar. 2024.
4. X. Cheng, J. Liu, K. Zheng, Z. Wu, L. Shi, and X. Hu, "Monitoring of damage evolution in carbon fiber reinforced polymer composites by electrical impedance tomography," *NDT & E International*, vol. 148, Art. no. 103239, Dec. 2024.
5. I. S. Akmanov, S. V. Lomov, M. Y. Spasennykh, and S. G. Abaimov, "Machine learning for crack detection in an anisotropic electrically conductive nano-engineered composite interleave with realistic geometry," *International Journal of Engineering Science*, vol. 205, Art. no. 104171, Dec. 2024.
6. G. Jovarauskaite, G. Monastyreckis, L. Mishnaevsky Jr., and D. Zeleniakiene, "Self-sensing composites with damage mapping using 3D carbon fibre grid," *Composites Part B: Engineering*, vol. 295, Art. no. 112182, Apr. 2025.
7. M. Dong, E. Bilotti, H. Zhang, C. S. Boland, and D. G. Papageorgiou, "High performing piezoresistive MoS, epoxy strain sensors for structural health monitoring," *Polymer*, vol. 309, Art. no. 127449, Sep. 2024.
8. M. Zarzoso, A. Mikhalchan, D. Mocerino, P. Romero-Rodriguez, R. Losada, J. J. Vilatela, and C. González, "Strain sensing of structural composites by integrated piezoresistive CNT yarn sensors," *Composites Part B: Engineering*, vol. 286, Art. no. 111752, Nov. 2024.
9. Y. Wang, B. Du, Y. Chen, X. Lin, and X. Kong, "Electrical insulation and dielectric properties of aramid fiber reinforced epoxy composites under mechanical stress," *Composites Science and Technology*, vol. 255, Art. no. 110733, Aug. 2024.
10. P. Gupta, E. Ruzicka, B. C. Benicewicz, R. Sundararaman, and L. S. Schadler, "Dielectric Properties of Polymer Nanocomposite Interphases Using Electrostatic Force Microscopy and Machine Learning," *ACS Applied Electronic Materials*, vol. 5, no. 2, pp. 794–802, Jan. 2023.
11. Ç. F. Özgenel, "Concrete Crack Images for Classification," *Mendeley Data*, **v2**, Jul. 2019.
12. Raja MR, Krishnan GH, Mohammad A, Cheerla S. Dual temporal gated multi-graph convolution network based neurodegenerative disease detection and severity prediction. *Biomedical Signal Processing and Control*. 2026;112(Pt A):108566.
13. Nesteena KN, Krishnan GH, Parthiban V, Krishna S, Sarkar S. In Silico Identification of 9-Amino Camptothecin as a Dual Inhibitor of VEGF-A and VEGF-B in N1–N8 Breast Cancer. *Biotechnology and Applied Biochemistry*. 2025 Oct 28. Online ahead of print.
14. Mohandass G, Sridhathan C, Krishnan GH, Nandhini I. Optimized dense back-projection joint attention network for automatic seizure detection from EEG signal. *Computer Methods in Biomechanics and Biomedical Engineering*. 2025. Published online (Nov 2025).
15. Krishnan GH, Sheeba S, Mohandass G, Kumar NMG, Reddy MRP. Automated Blood Cell Counting and Disease Identification Using Image Processing: Implications for Polymer Composite-Based Biomedical Diagnostic Devices. *Journal of Polymer and Composites*. 2025;13(06):262–270.

16. Krishnan GH, Umashankar G, Sheeba S, Reddy MRP, Prasanth BV. Dual-Stream Deep Learning Framework for Brain CT Image Classification and Implications for Polymer Composite Neuro Implant Evaluation. *Journal of Polymer and Composites*. 2025;13(06):172–179.
17. Krishnan GH, Mohandass G, Umashankar G, Reddy MRP, Ravindra G. AI-Assisted Defect Detection in Polymer Composite Insulators Using an Optimised Ensemble Deep Learning Framework for Structural Health Monitoring. *Journal of Polymer and Composites.* 2025;13(05).
18. Mohandass G, Krishnan GH, Selvaraj D, Sridhathan C. Lung Cancer Classification using Optimized Attention-based Convolutional Neural Network with DenseNet-201 Transfer Learning Model on CT image. *Biomedical Signal Processing and Control*. 2024 Sep;95:106330.
19. G. H. Krishnan, S. Prabhu, M. Himabindu, N. V. Karthikeya Reddy, S. Mounika and S. Santhosh, "Comparative Analysis Fault Detection in HT Electrical Insulators using Modified Transfer Learning based ResNet50, EfficientNetB0, and VGG16 through Image Processing," *2024 10th International Conference on Electrical Energy Systems (ICEES)*, Chennai, India, 2024, pp. 1-5.
20. Umashankar G, Krishnan GH, Sudhakar T, Mohandass G, Devaraju T, Devika V, Banu SS. Eye Blink Based Biometric Authentication System. In: *2023 International Conference on Bio Signals, Images, and Instrumentation (ICBSII)*. 2023:1–4.
21. Krishnan GH, Sukanya K, Sainath Reddy JS, Surya Prakash Reddy KS, Niharika N, Siva Sai Kiran MS. CNN based image processing for crack detection on HT insulator's surface. In: *2023 International Conference on Sustainable Computing and Smart Systems (ICSCSS).* 2023:618–621.
22. U. Ganesan, N. E. Edwin Paul, G. Hari Krishnan, S. Aarthi and I. Kumara Swamy, "Detecting Diabetes Mellitus from Tongue Image Hybrid Features and Neural Netowrk Classifier," *2022 IEEE 4th International Conference on Cybernetics, Cognition and Machine Learning Applications (ICCCMLA),* Goa, India, 2022, pp. 425-427,
23. Santhosh S, Juliet AV, Krishnan GH. Predictive analysis of identification and disease condition monitoring using bioimpedance data. *Journal of Ambient Intelligence and Humanized Computing*. 2021;12(2):2955–2963.
24. Santhosh S, Vimala Juliet A, Krishnan GH. Simulation of Signal Generation and Measuring Circuit and Real Time IoT Based Electrical Bio Impedance Cardiac Monitoring System. In: Pandian A, Ntalianis K, Palanisamy R, eds. *Intelligent Computing, Information and Control Systems (ICICCS 2019)*. Advances in Intelligent Systems and Computing. Vol 1039. Springer; 2020:701–706.
25. Sudhakar T, Hari Krishnan G, Santosh S, Meenakshi S, Thomas L. Prosthetic arm control using processing device, a comparative approach. *Biomedical Research*. 2018;29(13):2906–2911.
26. Krishnan H, Natarajan RA, Nanda A. Impact of upper limb joint fluid variation on inflammatory diseases diagnosis. *Journal of Electrical Engineering & Technology*. 2014;9(6):2114–2117.
27. Krishnan GH, Natarajan RA, Nanda A. Microcontroller based non invasive diagnosis of knee joint diseases. In: *2014 International Conference on Information Communication and Embedded Systems (ICICES)*. 2014:1–5.
28. Guru Anand V, Hari Krishna G, Mohandass G, Hemalatha RJ, Sundaram S. Predicting grade of prostate cancer using image analysis software. In: Proceedings of the 2nd International Conference on Trendz in Information Sciences & Computing (TISC-2010). 2010:122–124.
29. K. Manickaraj, R. Thirumalaisamy, S. Palanisamy, N. Ayrilmis, E. E. Massoud, M. Palaniappan, and S. L. Sankar, "Value-added utilization of agricultural wastes in biocomposite production: Characteristics and applications," Ann. N. Y. Acad. Sci., vol. 1549, no. 1, pp. 72–91, Jul. 2025. doi: 10.1111/nyas.15368.
30. S. Palanisamy, M. Kalimuthu, S. Dharmalingam, A. Alavudeen, R. Nagarajan, S. O. Ismail, S. Siengchin, F. Mohammad, and H. A. Al-Lohedan, "Effects of fiber loadings and lengths on mechanical properties of Sansevieria Cylindrica fiber reinforced natural rubber biocomposites," Mater. Res. Express, vol. 10, no. 8, p. 085503, Aug. 2023. doi: 10.1088/2053-1591/acefb0.
31. M. Palaniappan, S. Palanisamy, T. Murugesan, S. Tadepalli, R. Khan, S. Ataya, and C. Santulli, "Influence of washing with sodium lauryl sulphate (SLS) surfactant on different properties of ramie fibres," BioResources, vol. 19, no. 2, pp. 2609–2625, 2024. doi: 10.15376/biores.19.2.2609-2625.

32. R. Ramasubbu, A. Kayambu, S. Palanisamy, and N. Ayrilmis, “Mechanical properties of epoxy composites reinforced with Areca catechu fibers containing silicon carbide,” BioResources, vol. 19, no. 2, pp. 2353–2370, 2024. doi: 10.15376/biores.19.2.2353-2370.
33. N. Ayrilmis, G. Kanat, E. Yildiz Avsar, S. Palanisamy, and A. Ashori, “Utilizing waste manhole covers and fibreboard as reinforcing fillers for thermoplastic composites,” J. Reinf. Plast. Compos., vol. 44, no. 17–18, pp. 1108–1118, Sep. 2025. doi: 10.1177/07316844241238507.
34. B. Mylsamy, K. Aruchamy, S. K. M. Shanmugam, S. Palanisamy, and N. Ayrilmis, “Improving performance of composites: Natural and synthetic fibre hybridisation techniques in composite materials – A review,” Mater. Chem. Phys., vol. 334, p. 130439, Apr. 2025. doi: 10.1016/j.matchemphys.2025.130439.

